# Nonlinear finite-difference time-domain modeling of linear and nonlinear corrugated waveguides

**Richard W. Ziolkowski and Justin B. Judkins**

*Electromagnetics Laboratory, Department of Electrical and Computer Engineering, The University of Arizona, Tucson, Arizona 85721*

Received July 2, 1993; revised manuscript received April 25, 1994

A multidimensional, nonlinear finite-difference time-domain (NL-FDTD) simulator, which is constructed from a self-consistent solution of the full-wave vector Maxwell equations and dispersive (Lorentz), nonlinear (finite-time-response Raman and instantaneous Kerr) materials models, is used to study finite-length, corrugated, optical waveguide output couplers and beam steerers. Multiple-cycle, ultrashort-optical-pulse interactions with these corrugated, nonlinear, dispersive waveguides are characterized. An all-optical nonlinear beam-steering device is designed, and its output-coupling performance is characterized with this NL-FDTD simulator.

## 1. INTRODUCTION

With the continuing and heightened interest in linear and nonlinear semiconductor and optically integrated devices, more-accurate and -realistic numerical simulations of these devices and systems are in demand. Such calculations provide a testbed in which one can investigate new basic scientific and engineering concepts, materials, and device configurations before they are fabricated. The process from device conceptualization to fabrication and testing should therefore be enormously improved with numerical simulations that incorporate more-realistic models of the linear and the nonlinear material responses and the actual device geometries. It is felt that vector and higher-dimensional properties of Maxwell's equations (e.g., polarizations, reflections, longitudinal field effects, and transverse power flows) that are not currently included in existing scalar approaches, such as traditional beam-propagation methods and nonlinear-Schrödinger- (NLS) equation methods, in addition to more-detailed materials models, may significantly affect the scientific and engineering results.

We have numerically constructed solutions to the multidimensional, full-wave, vector Maxwell equations describing the interaction of ultrashort pulsed beams with a dispersive nonlinear material having a finite response time. These numerical solutions have been obtained[1–4] in two space dimensions and time with a nonlinear finite-difference time-domain (NL-FDTD) method that combines a generalization of a standard finite-difference time-domain (FDTD), full-wave, vector, linear Maxwell equations solver with a Lorentz linear dispersion model, a nonlinear (thermal) Raman model, and an instantaneous Kerr model. In particular, we are solving in a self-consistent manner the following system of equations:

$$\frac{\partial}{\partial t}[\mu_0 \mathbf{H}] = -\nabla \times \mathbf{E}, \tag{1}$$

$$\frac{\partial}{\partial t}[\epsilon_0 \mathbf{E}] = \nabla \times \mathbf{H} - \frac{\partial}{\partial t}\mathbf{P}, \qquad \text{Maxwell curl equations;} \tag{2}$$

$$\frac{\partial^2}{\partial t^2}\mathbf{P}^{\mathrm{L}} + \Gamma_L \frac{\partial}{\partial t}\mathbf{P}^{\mathrm{L}} + {\omega_L}^2 \mathbf{P}^{\mathrm{L}} = \epsilon_0 \chi_0 {\omega_L}^2 \mathbf{E}, \qquad \text{Lorentz model;} \tag{3}$$

$$\frac{\partial^2}{\partial t^2}\chi^{\mathrm{NL}} + {\omega_R}^2\left(\tau_R \frac{\partial}{\partial t}\chi^{\mathrm{NL}} + \chi^{\mathrm{NL}}\right) = \epsilon_R {\omega_R}^2 |\mathbf{E}|^2, \qquad \text{Raman model;} \tag{4}$$

where the polarization $\mathbf{P} = \mathbf{P}^{\mathrm{L}} + \mathbf{P}^{\mathrm{NL}}$ is composed of the linear contribution $\mathbf{P}^{\mathrm{L}}$ and the nonlinear contributions

$$\mathbf{P}^{\mathrm{NL}} = \epsilon_0 \chi^{\mathrm{NL}} \mathbf{E} + \epsilon_0 \chi^{\mathrm{Kerr}} |\mathbf{E}|^2 \mathbf{E}, \tag{5}$$

with $\chi^{\mathrm{Kerr}}$ being the instantaneous Kerr susceptibility. The susceptibility $\chi^{\mathrm{NL}}$ encompasses all the retarded nonlinear effects. For simplicity only, we treat the nonlinearities as being thermal rather than electronic. Goorjian and co-workers[5–7] are developing a similar capability to model pulse propagation under the influence of linear and nonlinear dispersive, linear and nonlinear diffractive, and time-retardation effects in the medium.

By coupling the linear and the nonlinear dispersion models simultaneously, as well as using the natural boundary conditions arising from dielectric discontinuities, for example, at gratings and corrugated interfaces, we have the ability to design all-optical switching devices and beam steerers for ultrashort pulses. The NL-FDTD approach can readily handle complex realistic structures. This permits a thorough investigation of the wave propagation in the presence of complicated scatterers built into a nonlinear waveguiding structure. In contrast to standard approaches, such as the beam-propagation method, the NL-FDTD approach allows one to study the effects of the reflected and the longitudinal field components, which become significant when complex scatterers or nonlinearities are present, and the nonlinear coupling between the longitudinal and transverse components, which becomes significant depending on the polarization of the fields. For the straightforward one-dimensional or two-dimensional (2D) waveguide structures treated in

0740-3224/94/091565-11$06.00 

Refs. 5–7, the full-wave vector Maxwell results replicate those expected from NLS studies.[8] The NL-FDTD technique is, however, more potent than the NLS method; it can be applied to much more complex situations and can provide new information not obtainable with the standard linear–nonlinear modeling methods.

The NL-FDTD approach is not a panacea for all optical modeling problems. It is useful because it can straightforwardly incorporate complicated structures and all the relevant physics that one is willing to build into the material models. The Raman and instantaneous Kerr nonlinearities used in the current NL-FDTD simulator are idealized, phenomenological models, but they have been chosen because of their widespread use. Additionally, because of the bandwidth of the pulses that are used in the examples below, one could argue that more than one resonance line should be included in the models. Multiple-resonance Lorentz and Raman models could be designed to mimic the behavior of most materials. However, we typically choose not to run problems in which the optical pulses have frequency spectra that are centered directly on the resonance lines; these models simply absorb most of the energy presented to them and hence generally lead to only modest scattering results. More realistic multilevel atomic models of the materials can be incorporated into the NL-FDTD simulator; these models are currently under development in cooperation with John Arnold at Glasgow University. Despite the ability of the approach to handle complicated structures and material models, the NL-FDTD simulation model is memory and time bound. It is an explicit approach whose time step is connected to the spatial discretization through the Courant stability condition. The amount of memory required is directly proportional to the number of unknowns, which is determined by the number of grid cells and the number of equations in the combined field–material models. Finer spatial resolution or a more complex material model requires more memory and more time steps for a given time-record length. Even 2D problems dealing with nonlinear structures that are millimeters in size and with pulses that are picoseconds long and have wavelengths of the order of a micrometer are truly enormous and challenge the largest machines available today. Larger problems simply await larger simulation platforms. Despite the ability of the NL-FDTD approach to handle reasonably sized design problems of current interest, we emphasize below the design and simulation of futuristic output couplers and beam steerers, those appropriate for ultrashort optical pulses and are of the order of several wavelengths in size.

Corrugated waveguides are an example of a 2D scattering structure that requires inclusion of both the transverse and the longitudinal field components in its design. These structures have been of considerable interest in integrated optics because of their potential applications as couplers, converters, filters, or steering devices of the Bragg type. However, they have been analyzed mainly in the linear regime as infinite periodic structures[9–13] by use of Floquet mode theory. To design a useful nonlinear corrugated structure that is only a few wavelengths long for any of these applications, one must resort to a numerical modeling tool such as the NL-FDTD approach that allows the dielectric waveguide or the corrugations themselves to be nonlinear materials and allows for arbitrary groove spacings and depths, tapering of the corrugations, single-cycle or multiple-cycle pulses, and either TE or TM polarization. One rapidly realizes that the currently available analysis tools, such as the beam-propagation and NLS methods, cannot provide the desired results. The inadequacy of analytical approaches, such as perturbation techniques, even in the general linear case has been recognized.[11,12] In addition, the NL-FDTD approach permits one to visualize all the physical scattering processes involved in the interaction of the pulses with the corrugated structure. It is our aim in this paper to demonstrate the efficacy of using the NL-FDTD approach to design finite corrugated waveguide structures as output couplers and beam steerers for ultrashort pulses.

The NL-FDTD approach can handle single-cycle cases as readily as multiple-cycle cases that have an intrinsic carrier wave. Since most current optical systems deal directly with a carrier-wave-type signal, the NL-FDTD approach is used here to simulate the propagation and the scattering effects associated with those signals. It can also simulate the behaviors of single-cycle optical devices and systems as presented in Ref. 2. The single-cycle results represent behaviors that should be observed with optical systems currently under investigation and those being developed for future studies by the international optics community. However, in either case the full pulse is modeled with the NL-FDTD approach rather than only the envelope of the carrier wave, as it is with the NLS models. The increase in computational costs associated with the NL-FDTD approach over the NLS models is warranted by the corresponding increase in phase and vector information retained by the former and generally ignored or included only in an approximate sense in the latter. The NL-FDTD approach handles the corrugations directly without any of the standard assumptions that are necessitated by the beam-propagation or NLS method. This enhanced modeling capability of the NL-FDTD approach allows one to model and distinguish the effects that arise in both the single- and the multiple-cycle TE and TM polarization cases.

## 2. CORRUGATED WAVEGUIDE PROBLEM

We specifically present NL-FDTD results for the simulation and design of linear and nonlinear slab waveguiding structures that can be built with corrugated sections to provide efficient energy extraction and beam-steering mechanisms for ultrashort optical pulses. This is one example of the linear–nonlinear interface class of problems that we have been investigating with the NL-FDTD approach.[3,4] Interest in the corrugated waveguide problem follows from our desire to design wavelength-sized all-optical guided wave couplers and beam steerers. Expected efficiencies of conversion from the guided mode energy to the radiated field energy have been observed in the linear cases and reproduce the results reported by McLeod and Hawkins in Ref. 14. The corresponding nonlinear waveguiding structures have presented us with interesting challenges in their analysis and interpretation. Previous analyses[15–18] of related wave-

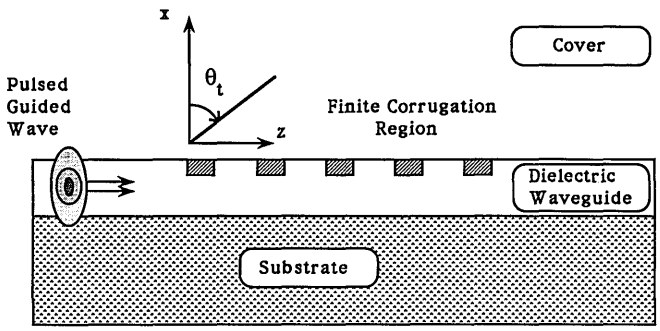


Fig. 1. NL-FDTD approach applied to linear or nonlinear dielectric waveguides with the indicated corrugation profiles. The corrugations are uniform, uniformly spaced, and present in the high-field region of the waveguide, extending into the interior of the guide. These corrugations are taken to be perfect conductors for all but cases TM-1 and TE-1.

guide corrugation problems dealt only with the case of nonlinear-dielectric teeth and have not considered the corrugations with metallic teeth that we have studied. Moreover, unlike those studies, the present analysis does not deal with a pump–probe configuration. We are simply looking at the possibility of efficiently coupling out energy from the waveguide in a particular direction. NL-FDTD simulations of potentially realistic device configurations are presented below.

The basic corrugated waveguide geometries that we have considered are illustrated by the generic configuration given in Fig. 1. A thin-film slab waveguide is sandwiched between two materials, the cover and the substrate. The corrugation region resides between the waveguide and the cover; it is excited by an incident waveguide mode. The teeth of the corrugations that we have studied have been both dielectric (similar dielectric teeth extended out of the dielectric waveguide or dissimilar linear and nonlinear dielectric teeth embedded in or on top of the waveguide) and metallic (embedded in or deposited on top of the dielectric waveguide). Various spacings of the corrugations and their lengths have been considered.

As is described in detail in Ref. 2, the NL-FDTD approach proceeds by discretizing space (in two dimensions) with a mesh of squares. The time is also discretized, with the spatial and temporal discretizations being specified by the Courant stability criterion. The electric and the magnetic field components, the linear polarization vector components, and the Raman nonlinear susceptibility are readily calculated with spatially and temporally centered, finite-difference approximations to the system of Eqs. (1)–(5). For the cases treated below a spatial discretization of $\Delta x = \Delta z = \lambda/30$ and a temporal discretization slightly below the 2D Courant condition, $\Delta t = 0.707(\Delta z/\sqrt{2}\,v)$, where $v$ is the maximum group velocity in any of the materials, were used. The presence of the physical loss terms in the material models relaxed the discretization requirements that we found in Ref. 2. This real-loss mechanism results in a numerical behavior that is analogous to the artificial-viscosity effects that one realizes with flux-conserving schemes in computational fluid-dynamics simulations.

The NL-FDTD problem is initiated at a specified planar aperture located within the simulation region with a modified total-field–scattered-field boundary that accounts for the presence of the dispersive nonlinear material. For the waveguide problems treated here this aperture is taken to be transverse to the direction of propagation, i.e., along the waveguide. The aperture is driven either with a pulsed $TE_0$ or a $TM_0$ waveguide mode; i.e., the initial transverse amplitude distribution in the source plane is taken to the value of the $TE_0$ or $TM_0$ mode there multiplied by a specified time signal. The total electromagnetic field is calculated from the source plane in the direction of propagation; the scattered fields are calculated at all points before the source plane. The simulation mesh is truncated at all its boundaries with second-order Mür conditions.[19] This approach minimizes the numerical artifacts that arise from the finite aperture (non-plane-wave) incident pulsed field and allows for backreflections from the corrugated structures through the source plane. The source plane is generally located near the left absorbing boundary to facilitate removal of this reflected power from the simulation region.

We refer to ultrashort pulses as those pulses that are single-cycle or multiple-cycle envelopes containing only a few cycles. Sources in the laboratory have produced pulses compressed to as short as four optical cycles. By using these sources we illustrate two advantages of the time-domain approach: (1) the ability to carry phase information over a wide spectrum and (2) the ability to model transient effects that occur either quickly or slowly relative to the time scale of the pulse. The evolution of the pulse in the medium can be dependent on both the material's resonances in the presence of the beam as well as the initial shape of the exciting pulse. Switching or steering of this type of pulsed beam in a wavelength-sized structure requires one to take advantage of interference effects and the materials' transient responses.

To initiate the simulations, we have used both a cw (or monochromatic) signal,

$$F(t) = \sin(2\pi t/T_p), \tag{6}$$

and a time-limited, multiple-cycle sine pulse given by the function

$$F(t) = \sin(2\pi t/T_p)(1 - x^2)^4 H(1 - |x|),$$
$$x = (2t - T_r)/T_r, \tag{7}$$

where $H(x)$ is Heaviside's function, $T_p$ is the optical period of the carrier, and $T_r$ is the time-record length of the pulse. Initial driving function (6) is continuous everywhere; initial driving function (7) is continuous and has at least its first two time derivatives continuous at the endpoints of the time interval $[0, T_r]$. For the corrugated waveguide cases in which there are $N_c$ periods of a unit cell whose characteristic length is $\Lambda$, we refer specifically to a short pulse as a signal whose equivalent length $v_G T_r$ is of the order of the entire corrugation length $N_c\Lambda$, i.e., $v_G T_r \lesssim N_c\Lambda$, where $v_G$ is the group velocity in the waveguide. Our shortest-pulse case that will be presented below contains 10 optical cycles over a corrugated waveguide section composed of 11 unit cells. This is a sufficient number of cycles for the pulse to be essentially a narrow-bandwidth cw signal and for the pulse train to span a distance smaller than the total corrugation length for a period of time. However, because of the $(1 - x^2)^4$

amplitude taper, this 10-cycle pulse has only ~6 cycles of nontrivial magnitude to be considered. Because the bandwidth increases as the number of cycles decreases, the effective frequency[20] of the signals seen by the corrugation section is slightly increased.

The corrugated waveguide with dielectric or metallic teeth can be viewed as a leaky-wave antenna. The corrugation section is a slow-wave structure whose impedance properties determine the properties of its radiated fields. The field radiated by an infinite linear or nonlinear corrugated structure can be modeled with a Floquet mode representation. The resulting fields have to satisfy a phase-matching or Bragg condition resulting from the electromagnetic boundary conditions. Physically this means that because of the regular placement of the teeth in the corrugation section the individual scattered fields will interfere constructively only along certain preferred directions, and the leaked energy will appear in the form of pulsed beams that radiate at angles specified by the Bragg condition both into the cover and into the substrate regions.

In particular, let $\theta_t$ be the angle that the radiated beam subtends with respect to the normal of the waveguide, $n_0$ be the index of refraction in the region outside of the guide adjoining the corrugations, and $n_G = n_B + n_2 I$ be the index of refraction in the waveguide, which includes the effective waveguide index $n_B$ (which varies slightly from the TE and TM cases to achieve the desired $TE_0$ and $TM_0$ initial spatial amplitude distributions) and the intensity-induced index change $n_2 I$. This Bragg condition then takes the form

$$\frac{\omega}{c} n_0 \sin\theta_t = \frac{\omega}{c} n_G + m\frac{2\pi}{\Lambda}, \quad \text{where } m = 0, \pm 1, \pm 2, \ldots,$$

or

$$\theta_t = \sin^{-1}\left(\frac{n_B}{n_0} + \frac{n_2}{n_0} I + m\frac{\lambda}{n_0 \Lambda}\right), \quad \text{where } m = 0, \pm 1, \pm 2, \ldots. \quad (8)$$

This immediately translates into a practical device: the output beam from the corrugation section can be steered away from the normal by the strength of the intensity of the input waveguide pulsed beam, the size of the unit cell, or the strength of the nonlinearity. For all the cases considered below the first-order beam is given by the $m = -1$ value.

A special case of this relationship suggests the design denoted below as geometry 3. If we design the corrugation spacing so that $\Lambda = \lambda/n_B$, then the first-order ($m = -1$) output beam from the corrugation section of the waveguide has the transmission angle

$$\theta_t = \sin^{-1}\left(\frac{n_2}{n_0} I\right) \approx \frac{n_2}{n_0} I. \quad (9)$$

Thus the angle of the output beam from the corrugation section can be controlled directly by the choice of the parameters for the input waveguide pulsed beam or the waveguide material.

## 3. NUMERICAL RESULTS

A variety of $TE_z$ and $TM_z$ cases for the corrugated slab-waveguide configuration have been considered with our NL-FDTD simulator. There are 10 TM cases reported below, TM-1 to TM-10; there are eight corresponding TE cases, TE-1 to TE-6, TE-8, and TE-10. All but two of the TM and the TE cases use the driving signal of Eq. (6); cases TM-10 and TE-10 use the driving signal of Eqs. (7). In all these cases the initial spatial distributions are the corresponding $TM_0$ and the $TE_0$ even waveguide modes. The maximum electric-field value of the incident modes is normalized to unity, giving a peak intensity of 1.0 V/m. The nonlinear coefficients are normalized in a corresponding manner. The basic problem configuration dimensions are shown in Fig. 2. We refer to the specific geometries used, which are characterized by the unit cell length $\Lambda$, the number of unit cells in the corrugated section $N_c$, and the tooth height $h$ as

Geometry 1, $\Lambda = 0.20$ $\mu$m, $N_c = 6$, $h = 0.02$ $\mu$m;
Geometry 2, $\Lambda = 0.20$ $\mu$m, $N_c = 6$, $h = 0.04$ $\mu$m;
TE geometry 3, $\Lambda = 0.105$ $\mu$m, $N_c = 11$, $h = 0.02$ $\mu$m;
TM geometry 3, $\Lambda = 0.110$ $\mu$m, $N_c = 11$, $h = 0.02$ $\mu$m.

The waveguide thickness $d = 0.12$ $\mu$m; the tooth length $l = \Lambda/2.0$; the background index in the thin-film waveguide $n_f = \sqrt{2.0}$, giving the effective background indexes for guided mode propagation $n_B^{TM} = \sqrt{1.740}$ and $n_B^{TE} = \sqrt{1.804}$; and the substrate linear index and the cover linear index were set to the free-space value, $n_s = n_c = 1.0$.

In all cases the free-space cw wavelength of interest was taken to be $\lambda = 0.15$ $\mu$m. This choice of wavelength was made simply to permit comparisons with the linear results obtained by McLeod and Hawkins[14] and to extend them to the corresponding nonlinear regimes. The parameters were not chosen with a specific laser system or material in mind. Since the grating physics is determined in terms of relative wavelengths, many of the re-

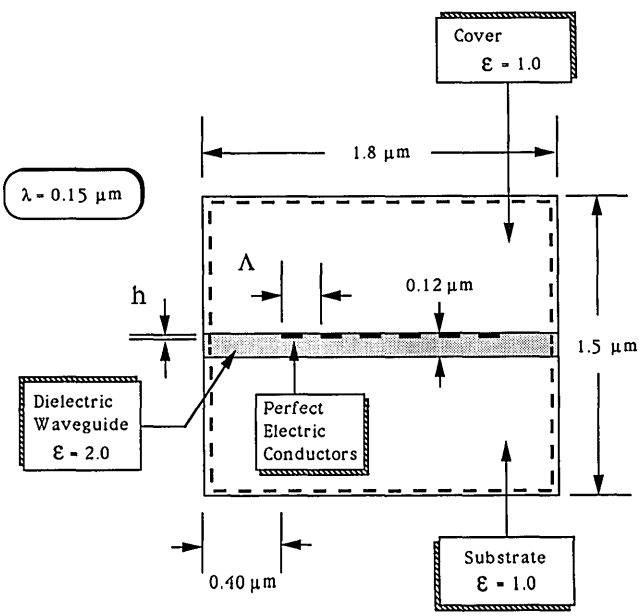


Fig. 2. NL-FDTD corrugated waveguide problem geometry. The various power sensor locations are indicated by dashed lines.

sults can be scaled to different frequency regimes with an appropriate change in the material parameters.

Within a specific dielectric waveguide configuration the nonlinear coefficients are varied from case to case to provide the desired comparisons. In addition we consider two compositions of the grating structure itself. In one configuration the teeth have the same dielectric properties as the cover, so they actually appear as gaps in the waveguide. In the other configuration the teeth of the corrugations are composed of perfect electric conductors. We found that the metal-teeth corrugations caused a much more efficient output coupling than the conventional dielectric-teeth (gap) case. As a result our studies have concentrated on the metallic corrugation cases. From linear theory the indicated value of the tooth length causes the TE and TM cases to radiate strongly in opposite directions as discussed below. Linear theory[12] also indicates that the leaked-energy coefficient should saturate if the tooth height is increased beyond the value $h = 0.2\ \lambda$. Additionally, since the electric-field behavior near the edges of the teeth is significantly different between the TE and TM polarizations, the resulting radiated field structures should reflect this difference. Note that the waveguide dispersion and the impedance caused by the presence of the corrugation are different for the different polarization and material cases. We found the fields radiated in the TM cases to be superior in quality to those generated in the TE cases, thus providing another reason to stress the TM configurations.

Cases TM-1 and TE-1 are linear slab-waveguide configurations that use geometry 1 and are the only cases that have dielectric teeth. Cases TM-2 and TE-2 are linear and are configured in geometry 1. Case TM-7 is also linear but configured in geometry 3. The waveguide is nonlinear in the remaining TM and TE cases. The susceptibility for the Lorentz dispersion model is 3.0 for dc and 0.0 at high frequencies. A single resonance is placed at $\omega_L = 3.5 \times 10^{15}$ rad/s, less than half the cw source radial frequency of $\omega = 12.57 \times 10^{15}$ rad/s, to cause a slight anomalous dispersion. The damping in the Lorentz model is negligibly small with $\Gamma_L = 2.0 \times 10^{10}\ \mathrm{s}^{-1}$. The nonlinear coefficients are $\epsilon_R = 0.15\ \mathrm{m}^2/\mathrm{V}^2$, and $\chi^{\mathrm{Kerr}} = 0.20\ \mathrm{m}^2/\mathrm{V}^2$ for the retarded and the instantaneous nonlinearities, respectively. The Raman resonance is taken to be $\omega_R = 8.197 \times 10^{13}$ rad/s; the Raman linewidth is determined by the term $\tau_R = 4.651 \times 10^{-15}\ \mathrm{s}^{-1}$. These material parameters yield a weak Raman interaction. The susceptibility obtained from the corresponding uniform-plane-wave Lorentz-dispersion model as a function of the frequency is given in Fig. 3(a); the analogous Raman model results are shown in Fig. 3(b). As expected from the parameter choices, the linewidths of the Lorentz and Raman models are extremely narrow. Nonetheless, the linear dispersion has an effect on the propagation behavior in the waveguide. In contrast the nonlinear behavior produced in this model is associated mainly with the instantaneous Kerr nonlinearity. Cases TM-3 and TE-3 represent the weak-Raman-interaction model version of geometry 1; cases TM-4 and TE-4 represent the weak-Raman-interaction model version of geometry 2. In cases TM-5 and TE-5 geometry 1 is considered again, but the thermal Raman interaction is now strong. To achieve this strong Raman interaction, we set the nonlinear material parameters to the values $\omega_R = 1.0 \times 10^{15}$ rad/s, $\tau_R = 0.5 \times 10^{-15}\ \mathrm{s}^{-1}$, $\epsilon_R = 0.15\ \mathrm{m}^2/\mathrm{V}^2$, and $\chi^{\mathrm{Kerr}} = 0.20\ \mathrm{m}^2/\mathrm{V}^2$. The susceptibilities obtained from the corresponding uniform-plane-wave Raman models are identical, apart from a scale factor, to those given in Fig. 3(b). In contrast to the weak-Raman-interaction model, the strong-Raman-interaction model is considerably broader. Thus, in addition to the instantaneous Kerr nonlinearity, the Raman interaction will also produce nontrivial contributions to the dispersive and the nonlinear behavior of the system in this case. Cases TM-6 and TE-6 deal with geometry 1, and both nonlinear indexes doubled to the values $\epsilon_R = 0.30\ \mathrm{m}^2/\mathrm{V}^2$ and $\chi^{\mathrm{Kerr}} = 0.40\ \mathrm{m}^2/\mathrm{V}^2$. Cases TM-8 and TE-8 treat geometry 3 with the strong Raman interaction of cases TM-4 and TE-4. Case TM-9 treats geometry 3 with a doubling of the nonlinear coefficients used in the strong-Raman-interaction case. Cases TM-10 and TE-10 again treat geometry 3 with the strong-Raman-interaction nonlinearity parameters but for a 10-cycle pulse, Eqs. (7), with a period $T_p = 0.5$ fs and a total record length $T_r = 5.0$ fs.

In each of the TM and the TE cases the power radi-

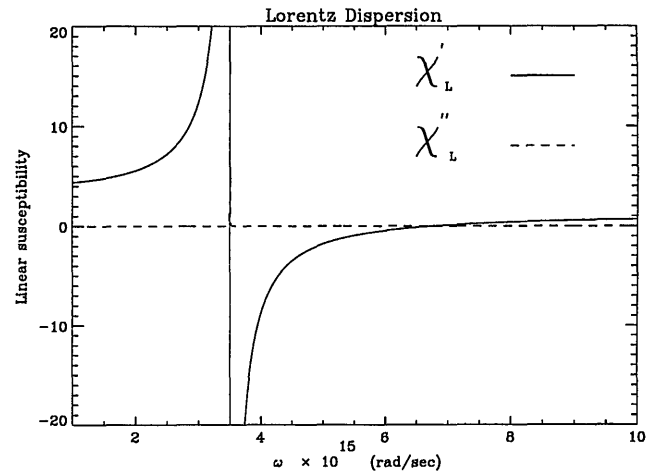


(a)

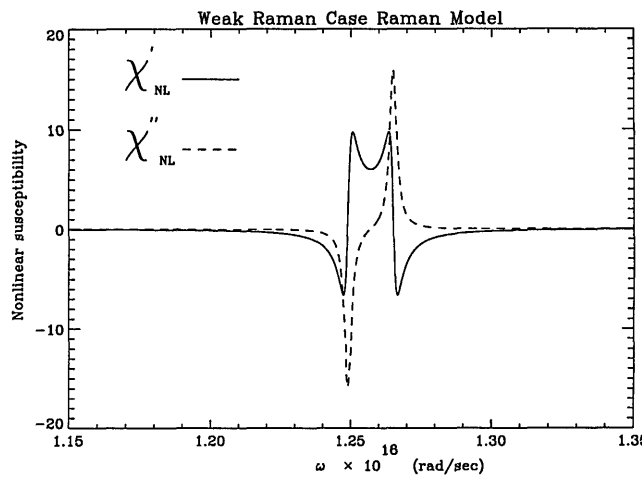


(b)

Fig. 3. Weak-Raman-interaction model susceptibilities. (a) Linear Lorentz model; (b) weak nonlinear Raman model.

ated through the boundaries of the simulation region indicated in Fig. 2 was monitored. The percentages of the total output power radiated into the cover, into the substrate, and reflected back along the waveguide from the corrugation section are listed in Tables 1 and 2 for all the cases reported here. In the cw cases these values represent the percentage per period; in the short-pulse cases it represents the total output energy (time-integrated output power). The output angles of the $m$th-order beams were calculated with a near-field-to-far-field transformation analogous to the one developed in Ref. 21. The radiated fields are collected over a plane in the simulation region at a specified transverse distance from the slab waveguide. These time histories are transformed into the frequency domain to yield the equivalent aperture fields, and the Fraunhaufer pattern is then obtained by use of the vector form of the Kirchhoff–Huygen representation.[22] For instance, in the TE cases we use the electric field at the collection plane $x = x_s$, which has the unit normal $\hat{n}_S = \hat{x}$ pointing into the cover, to obtain the far-field expression at $\mathbf{r}$:

$$\mathbf{E}(\mathbf{r}, \omega) = 2\nabla \times \int_S dS'[\hat{n}_s \times \mathbf{E}_{\text{aperture}}(\mathbf{r}', \omega)]G(\mathbf{r}, \mathbf{r}, \omega)$$

$$\approx \hat{y}\frac{\exp(ikR)}{\sqrt{\lambda R}}\exp(-i\pi/4)$$

$$\times\left\{\frac{x - x_s}{R}\int_{z_{\text{left}}}^{z_{\text{right}}} dz' E_y(x_s, z')\exp[-ik(z/R)z']\right\}, \quad (10)$$

where we use the approximate form of the 2D Green's function $G(\mathbf{r}, \mathbf{r}', \omega) = (i/4)H_0^{(1)}(\omega|\mathbf{r} - \mathbf{r}'|/c)$ and the distance $R = [(x - x_s)^2 + z^2]^{1/2}$ and have integrated over the simulation region plane $x = x_s$ from its left boundary $z_{\text{left}}$ to its right boundary $z_{\text{right}}$. Identifying the angle $\theta$ with respect to the normal $\hat{n}_S$ as $\sin\theta = z/R$, we obtain the far-field pattern immediately from the expression in the braces. The numerically calculated output angles of the first-order beams are also listed in Tables 1 and 2. In the short-pulse cases TM-10 and TE-10 the angles listed represent the angles of the estimated phase fronts in the output beams measured with a ruler and protractor. We are currently implementing the corresponding time-domain near-field-to-far-field transformation from Ref. 21 for more accurate measurements of the output angles in these short-pulse cases.

The basic field behavior obtained in the weakly nonlinear cases TM-3 and TE-3 is illustrated with the total electric-field intensity plots given in Figs. 4(a) and 5(a). Each plot is a snapshot of the intensity distribution at approximately the same time in the simulation. Brief computer movies of the data allow one to watch the field evolution over the entire time-record length of interest. The significant differences in output radiation behaviors are immediately apparent in these single snapshots. The majority of the power is radiated up into the cover region in the TM case and down into the substrate in the TE case. One can see, as is expected from the phase-matching condition (8), that multiple beams are generated both above

**Table 1. Coupling Efficiencies and Output Angles for the Various TM Polarization Cases**

| Simulation Case | Above (%) | Below (%) | Back-reflection (%) | Output Angle (deg) |
|---|---|---|---|---|
| TM-1: Geometry 1, linear guide, dielectric teeth | 2.5 | 2.3 | 0.30 | 34.5 |
| TM-2: Geometry 1, linear guide, metallic teeth | 44.2 | 11.4 | 13.1 | 36.7 |
| TM-3: Geometry 1, NLWG with weak Raman interaction | 44.2 | 11.0 | 9.8 | 38.3 |
| TM-4: Geometry 2, NLWG with weak Raman interaction | 45.8 | 30.4 | 19.2 | 37.0 |
| TM-5: Geometry 1, NLWG with strong Raman interaction | 45.3 | 11.2 | 12.6 | 39.1 |
| TM-6: Geometry 1, NLWG with weak Raman interaction and factor-of-2 increase in all nonlinear indexes | 42.3 | 11.0 | 12.6 | 39.3 |
| TM-7: Geometry 3, linear guide | 28.0 | 3.4 | 14.4 | −1.6 |
| TM-8: Geometry 3, NLWG with strong Raman interaction | 26.8 | 3.3 | 9.3 | 1.8 |
| TM-9: Geometry 3, NLWG with strong Raman interaction and factor-of-2 increase in all nonlinear indexes | 35.3 | 4.8 | 18.7 | 3.5 |
| TM-10: Geometry 3, NLWG with strong Raman interaction, short-pulse case | 49.3 | 8.6 | 5.2 | −4.0 |

**Table 2. Coupling Efficiencies and Output Angles for the Various TE Polarization Cases**

| Simulation Case | Above (%) | Below (%) | Back-reflection (%) | Output Angle (deg) |
|---|---|---|---|---|
| TE-1: Geometry 1, linear guide, dielectric teeth | 4.3 | 4.6 | 0.06 | 36.3 |
| TE-2: Geometry 1, linear guide, metallic teeth | 15.4 | 37.2 | 4.9 | 34.7 |
| TE-3: Geometry 1, NLWG with weak Raman interaction | 14.3 | 21.6 | 13.5 | 36.5 |
| TE-4: Geometry 2, NLWG with weak Raman interaction | 7.6 | 49.3 | 14.6 | 33.5 |
| TE-5: Geometry 1, NLWG with strong Raman interaction | 14.8 | 26.5 | 3.3 | 39.3 |
| TE-6: Geometry 1, NLWG with weak Raman interaction and factor-of-2 increase in all nonlinear indexes | 13.7 | 22.9 | 5.3 | 40.3 |
| TE-8: Geometry 3, NLWG with strong Raman interaction | 19.8 | 33.2 | 5.8 | 4.2 |
| TM-10: Geometry 3, NLWG with strong Raman interaction, short-pulse case | 14.1 | 30.8 | 6.0 | −4.0 |

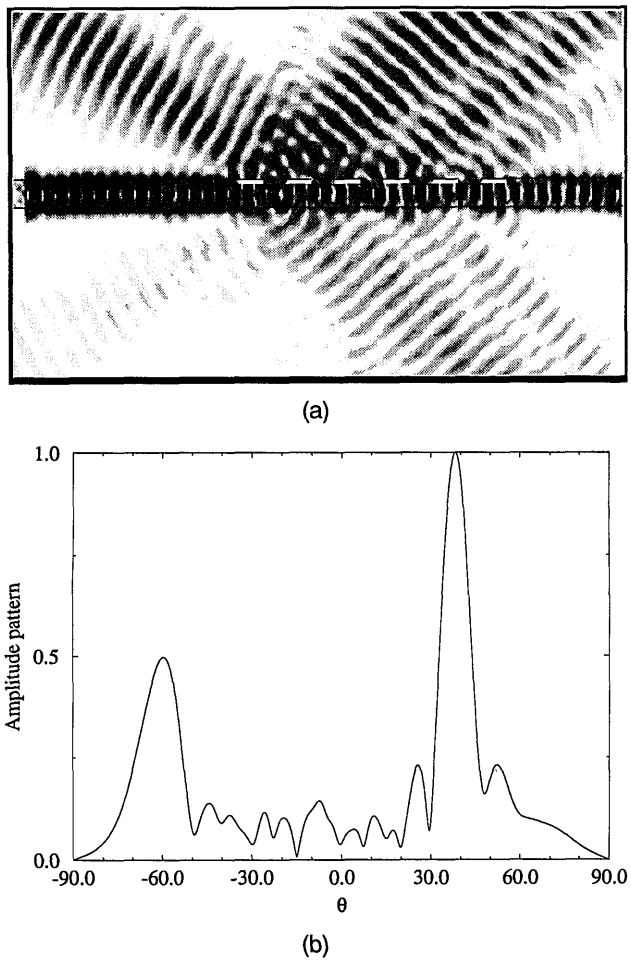


Fig. 4. (a) Electric-field intensity plots for the TM weak Raman interaction, geometry 1, case TM-3. (b) Corresponding far-field pattern. The Bragg angles correspond to the peaks that occur at the angles 38.3° and −59.5°.

and below the corrugation section. This is further confirmed with the corresponding far-field patterns shown in Figs. 4(b) and 5(b). Much of the initial radiation can actually be seen in the simulations as arising from the incident field with the first metallic corner. The interaction of the incident waveguide field with consecutive teeth provides a set of coherent sources that creates the resulting output beams.

One main difference between driving the specified corrugated waveguide sections with the $TM_0$ and the $TE_0$ waveguide modes is that the TM device prefers to couple light into beams (see Figs. 2, 4, and 5) that radiate into the cover region (adjacent to the corrugations), whereas the TE device prefers to couple light into beams that radiate into the substrate region (opposite the corrugations). Since we were consciously trying to enhance the output coupling, the teeth were positioned within the interior of the dielectric waveguide rather than on its exterior. This placement caused a larger interaction between the teeth and the incident modes. The other main difference between the TM- and the TE-polarization cases is that energy is radiated out of the waveguide region into the preferred beam directions more efficiently in the TM case.

These polarization-sensitive properties of the corrugated structure arise because in the TE case there is a node along the conductor (i.e., $E_y$ must be zero) and in the TM case there is an antinode (i.e., $E_x$ is maximum, a singular value, at the corner of the teeth). Thus in the TE case the openings between the teeth in the corrugation act as waveguides below or near cutoff, deflecting power down away from them into the substrate rather than up through them into the cover region. The TM mode, on the other hand, sees just the opposite conditions; large fields exist in those waveguides between the teeth without a cutoff frequency. A small dipole array is formed, and power then is readily coupled into a well-defined beam propagating away from the corrugations into the cover region.

Nonlinearities in the waveguide further enhance the differentiation between the two polarization cases. The output coupling for the TE cases decreases with increasing nonlinearity, but it remains approximately unchanged for the TM cases. The reason for this behavior is that the field distribution in the nonlinear waveguide becomes more confined as the nonlinearity is increased. The TE field is then pulled away from the corrugation toward the substrate side of the waveguide, where the field intensity is strongest and thus is affected less strongly by the corrugation. The TM field also experiences a similar localization effect. However, the increased nonlinearity also

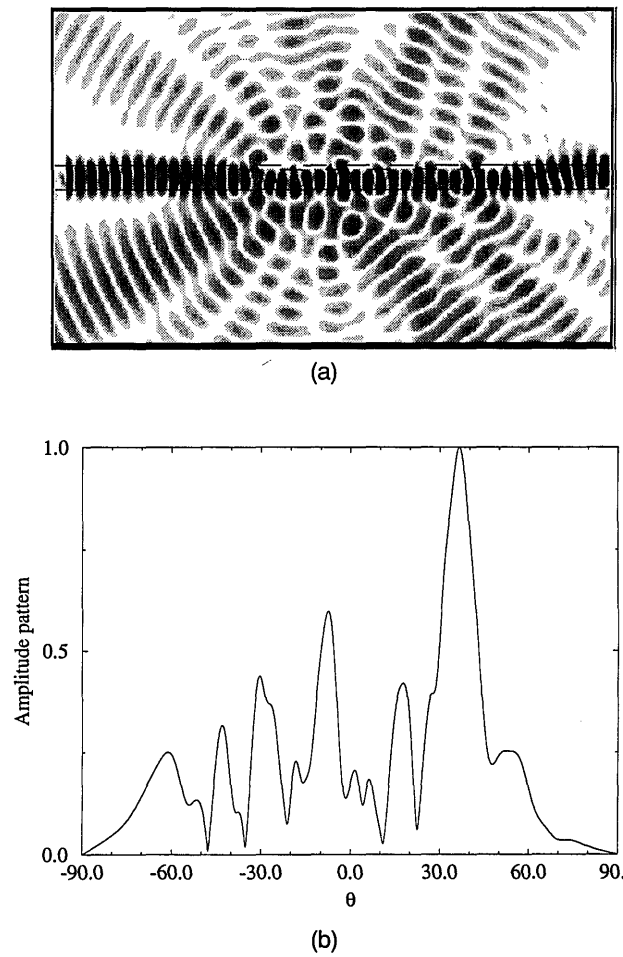


Fig. 5. (a) Electric-field intensity plots for the TE weak Raman interaction, geometry 1, case TE-3. (b) Corresponding far-field pattern. The Bragg angles correspond to the peaks that occur at the angles 36.5°, −7.6°, and −61.0°.

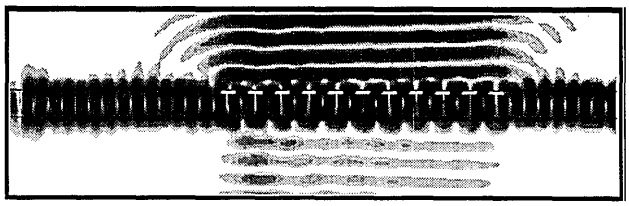

(a)

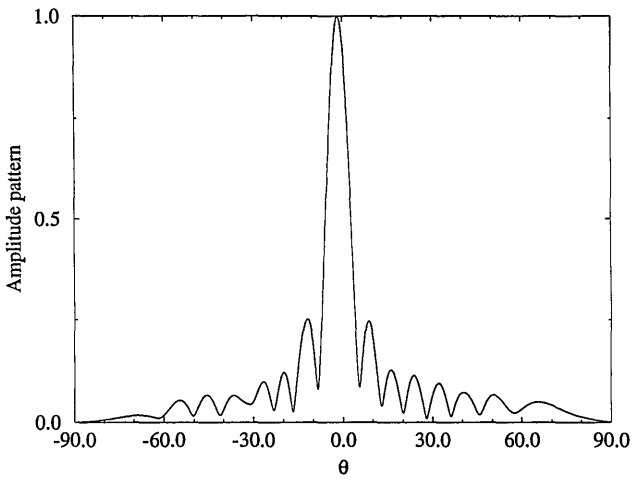


(b)

Fig. 6. (a) Electric-field intensity plots for the TM linear interaction, geometry 3, case TM-7. (b) The corresponding far-field pattern. The peak occurs at the angle −1.6°.

increases the field levels near the edges of the teeth, compensating for the decrease in the incident field strength. Hence the TM mode remains strongly coupled to the corrugation. Additional coupling is further retarded as the nonlinearity is increased because the field begins to form a channel, and the remaining power in the waveguide is trapped by it.

The simulation cases all indicate that nonlinear-waveguide (NLWG) corrugation sections are reasonably good output-coupling and beam-steering devices. They also suggest that these NLWG corrugation sections can act as extremely good polarization-differentiating devices as well. To facilitate a strong coupling of energy out of the waveguide in a short distance, all the corrugation cases constructed with the metallic teeth outperformed dielectric corrugation cases TM-1 and TE-1. The coupling efficiency in the former cases is increased dramatically, more than an order of magnitude, over the latter cases. Note that, for the dielectric grating, TE-polarization case TE-1 gave slightly more output coupling than TM-polarization case TM-1. The conducting corrugation TE-mode devices direct ~25% of the output power into the substrate region, whereas the corresponding TM-mode devices direct ~45% of the output power into the cover region. Beams that are smaller in amplitude are also produced that propagate at the same angles to the waveguide but in the opposite regions. There is some backward-propagating power in all cases, since the corrugated section acts as an impedance mismatch in the waveguide. The greater corrugation depth treated in cases TM-4 and TE-4 provided indications that the guided wave and the output beams become badly distorted when the teeth are too deep. The effect caused by doubling the tooth depth is to pinch off the power through the guide and to increase the reflected power. This results, of course, because the teeth cause a stronger perturbation of the incident guided mode.

Geometry 3, in which the grating periodicity is made to be equal to $\lambda/n_B$, provided the most interesting corrugated-waveguide device results. The expectation was to have the corrugation couple light out of the waveguide into a single beam at nearly 90° with respect to the guide. Moreover, because the term $\lambda/\Lambda < 1$, only the first-order ($m = -1$) beam is produced. In addition, this configuration provides the maximum sensitivity of the output-beam angle to the nonlinearity. Although the TE and the TM coupling performance in total output power was comparable, the TM beams were much more coherent and well behaved. The total electric-field intensity plots in cases TM-7 and TM-8 are given in Figs. 6(a) and 7(a), respectively. The corresponding patterns are given in Figs. 6(b) and 7(b), respectively. It is clear from these plots that increasing the nonlinearity does in fact change the output-beam direction. Several-degree beam shifts are easily obtained, as is indicated in these figures and in Table 1. The output angle in the linear TM-7 case is not exactly 0° only because we choose to maintain the same grid cell size for all the problems. The specific unit cell size needed for an exact match to achieve a 0° output beam does not correspond to an integer multiple of the unit discretization cell length. The total electric-field intensity plots for the TM and TE short-pulse cases

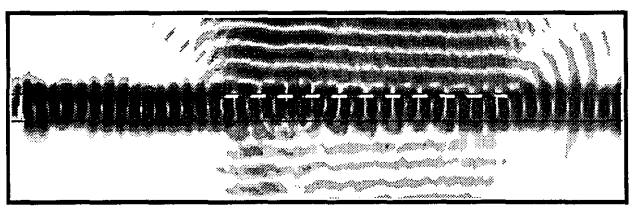

(a)

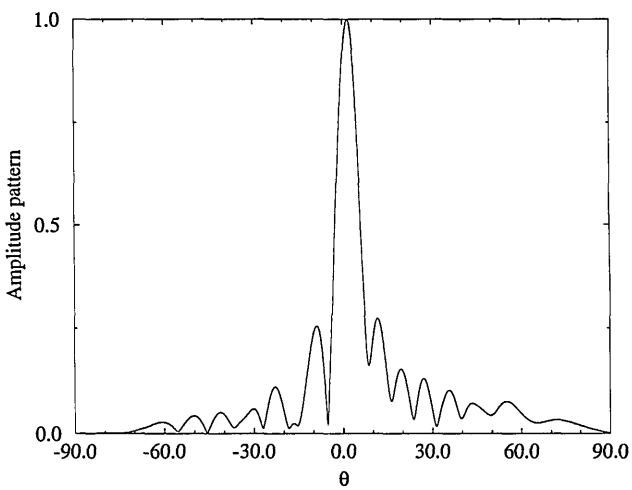


(b)

Fig. 7. (a) Electric-field intensity plots for the TM strong Raman interaction, geometry 3, case TM-8. (b) The corresponding far-field pattern. The peak occurs at the angle +1.8°.

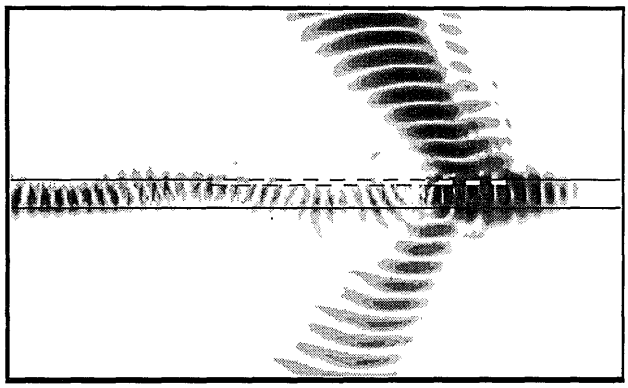

Fig. 8. Electric-field intensity plots for the short-pulse, TM strong Raman interaction, geometry 3, case TM-10.

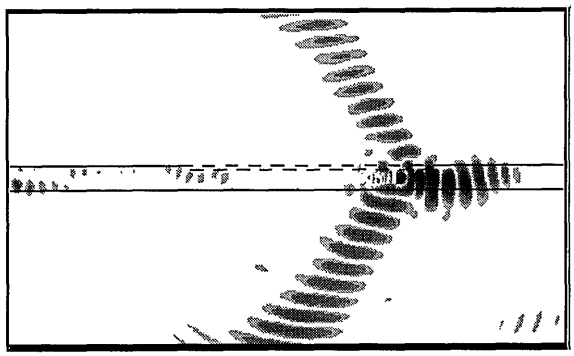

Fig. 9. Electric-field intensity plots for the short-pulse, TE strong Raman interaction, geometry 3, case TE-1.

TM-10 and TE-10 are given, respectively, in Figs. 8 and 9. The beam quality shown is achieved approximately after the incident field has interacted with the first three teeth of the corrugation section; it is maintained until the beam stops interacting with the teeth in the corrugation section. The difficulty in accurately describing the output beam direction is apparent. The beam appears to have a main direction that is different from the constant-intensity wave normals. In cases TM-10 and TE-10 these directions are $-33°$ and $-4°$, respectively. This output-beam pattern is maintained as the pulse moves through the waveguide section. Moreover, as in the cw cases, the output power in the short-pulse cases is highly directed—into the cover region adjacent to the corrugations in the TM case and into the substrate region opposite the corrugations in the TE case. These results strongly suggest that geometry 3 could be used for the basic design of a highly sensitive beam-steering device based on the interaction of ultrashort optical pulses with an ultrasmall corrugated waveguide section.

We have found that the output angles determined with the numerically generated fields compare well with the values predicted from phase-matching conditions (8) and (9). For the linear dielectric gratings, cases TM-1 and TE-1, the expected output angles are 34.7° and 36.4°, respectively. The combined FDTD simulations and the near-field-to-far-field transformation yielded the output angles 34.5° and 36.3°, respectively, in good agreement ($<0.6\%$ difference) with the analytical values. Moreover, the patterns are as expected for a finite grating structure: the lowest-order response is due to a product of the Bragg response and that of a finite slab, $\sin(x)/x$ function, and the higher-order beams vary slightly from the expected Bragg response. These results agree with those previously reported for linear gratings.[23,24] The metallic and the nonlinear dielectric corrugations, however, represent significant perturbations to the effective index in the waveguide, $n_B$, used in those Bragg conditions. For the TM-2 and TE-2 cases the combined FDTD simulations and the near-field-to-far-field transformation yield the output angles 36.7° and 34.7°, respectively. These angles indicate that with the metallic teeth, the effective index of the TM and TE waveguides is actually $\sqrt{1.816}$ and $\sqrt{1.741}$, respectively. With these indexes and the cell sizes indicated for the TM geometry 3 cases, the output angle expected from Eq. (8) is $-0.92°$; this compares favorably with the corresponding calculated value, $-1.6°$. Similar difficulties are encountered with the nonlinear waveguide cases. The simulator output angles for cases TM-3 and TM-6 are 38.3° and 39.3°, respectively. Knowing the value for the TM-3 case, we use Eq. (8) to predict the value 39.6° for the TM-6 case. This represents only a 1.5% difference between the analytical and the numerical results. Similarly, the output angle for case TM-9 is nearly double the value for TM-8, as is expected from relation (9). Nonetheless, these angle values could not have been established from Eq. (8) or relation (9) without the initial numerical value for at least one nonlinear case. Thus these results strongly indicate the need for numerical methods, such as the NL-FDTD simulator. Even though they are extremely useful for indicating the expected trends of the device's behavior, one should not rely simply on analytical approximations based upon scalar diffraction theory to model these finite, wavelength-sized structures for any realistic device applications.

Another phenomenon associated with beams' being strongly coupled out of the guide in the TM geometry 3 is illustrated by case TM-9 and Fig. 10, which represents the field distribution before steady-state conditions have been reached. This phenomenon is that the output beam can be made to focus. In particular, the corrugated section coupled with the nonlinearity can be made to act as a chirped grating. This effect is caused when the incident mode in the waveguide becomes depleted quickly by radiation as the mode propagates through the corrugation section. This energy depletion results in a decrease in the field strength, so the nonlinear refractive index is reduced further along the corrugation section. The coupling angle will then vary according to location along the corrugation. Light is being scattered from the corrugations, so there is a greater electric-field intensity at the beginning of the corrugation than at the end. Thus, the Bragg output coupling angle $\theta_t$ is directed slightly more toward the propagation direction (positive angle with respect to the normal) at the beginning of the corrugation section than it is later in that section, where the reduced intensity causes the Bragg output coupling angle $\theta_t$ to be directed slightly more away from the propagation direction (negative angle with respect to the normal). This behavior is illustrated in Fig. 10. These results imply that one could design a tapered corrugation region that is tailored to yield any desired focusing properties. The tapering

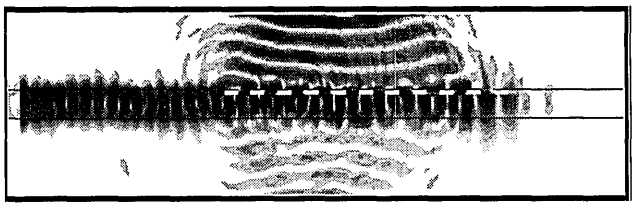

Fig. 10. Electric-field intensity plots for the TM strong Raman interaction, geometry 3, case TM-9, before steady-state conditions have been reached. With further detailed engineering design this configuration, combined with its beam-steering properties, could lead to an effective all-optical switch for short pulses.

could consist of varying the distribution of the nonlinear material in the waveguide or varying the unit cell widths along the corrugation section so that $\Lambda$ is varied from one unit cell to the next. If designed to encourage focusing, such an all-optical device could be used as a highly effective switch. This configuration is currently under investigation.

## 4. CONCLUSIONS

The application of the NL-FDTD approach to linear and nonlinear corrugated waveguides was presented. A variety of cases for both TE and TM polarizations were treated to illustrate the behavior of these waveguide structures as output couplers and beam steerers. Comparisons were made between the numerically predicted output-beam angles and those given by infinite structure analytical analyses. The results indicate the need for the numerical simulator when the device size is finite and of the order of a wavelength. The simulator was also used to model the interaction of ultrashort pulses with these corrugated structures. These results further indicate the need for the full-wave vector simulations.

The simulations indicated significant output coupling and usable beam-steering qualities for the corrugated structures, particularly when the corrugations are metallic and are embedded in the waveguide. The corrugated structures are polarization sensitive, the TM cases radiating the majority of the output power in a direction opposite to the TE cases. In one specific geometry the unit cell length was designed to give broadside emissions that were tunable by the magnitude of the intensity of the incident fields. An example of a focusing chirped grating structure was found; the chirped nature of the structure arises here from the nonlinearities. It is believed that with further design analyses with the NL-FDTD simulator a variety of corrugated linear and nonlinear waveguide structures could be developed for a large variety of practical applications.

## ACKNOWLEDGMENTS

This research was supported in part by the Lawrence Livermore National Laboratory under the auspices of the U.S. Department of Energy under contract W-7405-ENG-48. The authors also thank a reviewer for comments that led to an improved manuscript.

## REFERENCES

1. R. W. Ziolkowski and J. B. Judkins, "Optical nonlinear wake-field vortices: results from full-wave vector Maxwell equation simulations in two spatial dimensions and time," in *Integrated Photonics Research* (Optical Society of America, Washington, D.C., 1992), pp. 402–403.
2. R. W. Ziolkowski and J. B. Judkins, "Full-wave vector Maxwell equation modeling of the self-focusing of ultrashort optical pulses in a nonlinear Kerr medium exhibiting a finite response time," J. Opt. Soc. Am. B **10,** 186–198 (1993).
3. R. W. Ziolkowski and J. B. Judkins, "Linear–nonlinear interfaces: results from full-wave, vector Maxwell equation NL-FDTD simulations," in *Integrated Photonics Research* (Optical Society of America, Washington, D.C., 1993), pp. 128–131.
4. R. W. Ziolkowski and J. B. Judkins, "Applications of discrete methods to pulse propagation in nonlinear media: self-focusing and linear–nonlinear interfaces," Radio Sci. **28,** 901–911 (1993).
5. P. M. Goorjian and A. Taflove, "Direct time integration of Maxwell's equations in nonlinear dispersive media for propagation and scattering of femtosecond electromagnetic solitons," Opt. Lett. **17,** 180–182 (1992).
6. P. M. Goorjian, A. Taflove, R. M. Joseph, and S. C. Hagness, "Computational modeling of femtosecond optical solitons from Maxwell's equations," IEEE J. Quantum Electron. **28,** 2416–2422 (1992).
7. R. M. Joseph, P. M. Goorjian, and A. Taflove, "Direct time integration of Maxwell's equations in two-dimensional dielectric waveguides for propagation and scattering of femtosecond electromagnetic solitons," Opt. Lett. **18,** 491–493 (1993).
8. C. V. Hile and W. L. Kath, "Numerical and asymptotic solution of Maxwell's equations for nonlinear optical pulse propagation," in *Integrated Photonics Research* (Optical Society of America, Washington, D.C., 1993), pp. 308–311.
9. J. H. Harris, R. K. Winn, and D. G. Dalgoutte, "Theory and design of periodic couplers," Appl. Opt. **11,** 2234–2241 (1972).
10. K. Sakuda and A. Yariv, "Analysis of optical propagation in a corrugated dielectric structure," Opt. Commun. **8,** 1–8 (1973).
11. S. T. Peng, H. L. Bertoni, and T. Tamir, "Analysis of periodic thin-film structures with rectangular profiles," Opt. Commun. **10,** 91–94 (1974).
12. S. T. Peng, T. Tamir, and H. L. Bertoni, "Theory of periodic dielectric waveguides," IEEE Trans. Microwave Theory Tech. **MTT-23,** 123–133 (1975).
13. A. Hardy, "Exact derivation of the coupling coefficients in corrugated waveguides with rectangular tooth shape," IEEE J. Quantum Electron. **QE-20,** 1132–1139 (1984).
14. R. R. McLeod and R. J. Hawkins, "Using the finite difference time domain method as a design tool," in *Integrated Photonics Research* (Optical Society of America, Washington, D.C., 1992), pp. 38–39.
15. G. Assanto, G. I. Stegeman, and G. Vitrant, "Nonlinear all-optical beam scanner," Appl. Phys. Lett. **54,** 1854–1856 (1989).
16. G. Assanto and G. I. Stegeman, "Nonlinear all-optical beam scanner," J. Appl. Phys., **67,** 1188–1193 (1990).
17. J. E. Ehrlich, G. Assanto, and G. I. Stegeman, "All-optical tuning of waveguide nonlinear distributed feedback gratings," Appl. Phys. Lett. **56,** 602–604 (1990).
18. G. Assanto, "All-optical integrated nonlinear devices," J. Mod. Opt. **37,** 855–873 (1990).
19. G. Mür, "Absorbing boundary conditions for the finite-difference approximation of the time-domain electromagnetic-field equations," IEEE Trans. Electromagn. Compat. **EMC-23,** 377–382 (1981).
20. R. W. Ziolkowski and J. Judkins, "Properties of ultrawide-bandwidth pulsed Gaussian beams," J. Opt. Soc. Am. A **9,** 2021–2030 (1992).
21. M. J. Barth, R. R. McLeod, and R. W. Ziolkowski, "A near

and far-field projection algorithm for finite-difference time-domain codes," J. Electromagn. Waves Appl. **6,** 5–18 (1992).
22. J. A. Kong, *Electromagnetic Wave Theory* (Wiley, New York, 1986), pp. 376–396.
23. H. Shigesawa and M. Tsuji, "A new equivalent network method for analyzing discontinuity properties of open dielectric waveguides," IEEE Trans. Microwave Theory Tech. **37,** 3–14 (1989).
24. Q.-H. Liu and W. C. Chew, "Analysis of discontinuities in planar dielectric waveguides: an eigenmode propagation method," IEEE Trans. Microwave Theory Tech. **39,** 422–430 (1991).